Journal of Molecular and Cellular Cardiology 113 (2017) 9–21

Contents lists available at ScienceDirect

Journal of Molecular and Cellular Cardiology

journal homepage: www.elsevier.com/locate/yjmcc

Severe DCM phenotype of patient harboring RBM20 mutation S635A can be modeled by patient-specific induced pluripotent stem cell-derived cardiomyocytes

Katrin Streckfuss-Bömeke[a,b], Malte Tiburcy[b,c], Andrey Fomin[b,d], Xiaojing Luo[e], Wener Li[e], Claudia Fischer[a,b], Cemil Özcelik[f,g], Andreas Perrot[f], Samuel Sossalla[a,b,h], Jan Haas[i,j], Ramon Oliveira Vidal[k], Sabine Rebs[a], Sara Khadjeh[a,b], Benjamin Meder[i,j], Stefan Bonn[k,l], Wolfgang A. Linke[b,d], Wolfram-Hubertus Zimmermann[b,c], Gerd Hasenfuss[a,b], Kaomei Guan[a,e,*]

[a] Department of Cardiology and Pneumology, Universitätsmedizin Göttingen, Germany
[b] DZHK (German Center for Cardiovascular Research), Partner Site Göttingen, Germany
[c] Institute of Pharmacology and Toxicology, Universitätsmedizin Göttingen, Germany
[d] Department of Cardiovascular Physiology, Ruhr University Bochum, Germany
[e] Institute of Pharmacology and Toxicology, Technische Universität Dresden, Germany
[f] Cardiovascular Genetics, Experimental and Clinical Research Center, Charité-Universitätsmedizin Berlin, Germany
[g] Medizinischen Klinik I Kardiologie, Gastroenterologie und Diabetologie, Knappschaftskrankenhaus Recklingshausen, Germany
[h] Department of Internal Medicine 2 - Cardiology, University Medical Center Regensburg, Germany
[i] Department of Cardiology, University of Heidelberg, Germany
[j] DZHK, Partner Site Heidelberg, Germany
[k] German Center for Neurodegenerative Diseases, Göttingen and Tübingen, Germany
[l] Institute of Medical Systems Biology, Center for Molecular Neurobiology, University Clinic Hamburg-Eppendorf, Hamburg, Germany

ARTICLE INFO

Keywords:
RNA-binding motif protein 20 (RBM20)
Induced pluripotent stem cells (iPSCs)
Cardiomyocytes
Dilated cardiomyopathy (DCM)
Alternative splicing
Titin (TTN)

ABSTRACT

The ability to generate patient-specific induced pluripotent stem cells (iPSCs) provides a unique opportunity for modeling heart disease *in vitro*. In this study, we generated iPSCs from a patient with dilated cardiomyopathy (DCM) caused by a missense mutation S635A in RNA-binding motif protein 20 (RBM20) and investigated the functionality and cell biology of cardiomyocytes (CMs) derived from patient-specific iPSCs (RBM20-iPSCs). The RBM20-iPSC-CMs showed abnormal distribution of sarcomeric α-actinin and defective calcium handling compared to control-iPSC-CMs, suggesting disorganized myofilament structure and altered calcium machinery in CMs of the RBM20 patient. Engineered heart muscles (EHMs) from RBM20-iPSC-CMs showed that not only active force generation was impaired in RBM20-EHMs but also passive stress of the tissue was decreased, suggesting a higher visco-elasticity of RBM20-EHMs. Furthermore, we observed a reduced titin (TTN) N2B-isoform expression in RBM20-iPSC-CMs by demonstrating a reduction of exon skipping in the PEVK region of TTN and an inhibition of TTN isoform switch. In contrast, in control-iPSC-CMs both TTN isoforms N2B and N2BA were expressed, indicating that the TTN isoform switch occurs already during early cardiogenesis. Using next generation RNA sequencing, we mapped transcriptome and splicing target profiles of RBM20-iPSC-CMs and identified different cardiac gene networks in response to the analyzed RBM20 mutation in cardiac-specific processes. These findings shed the first light on molecular mechanisms of RBM20-dependent pathological cardiac remodeling leading to DCM. Our data demonstrate that iPSC-CMs coupled with EHMs provide a powerful tool for evaluating disease-relevant functional defects and for a deeper mechanistic understanding of alternative splicing-related cardiac diseases.

1. Introduction

Dilated cardiomyopathy (DCM) is a major cause of cardiovascular mortality, which is due to a progressive enlargement of the heart leading finally to heart failure. Only recently alternative splicing related cardiovascular diseases have been described [1]. *RBM20* codes for the

* Corresponding author at: Institute of Pharmacology and Toxicology, Technische Universität Dresden, Fetscherstraße 74, 01307 Dresden, Germany.
E-mail address: kaomei.guan@tu-dresden.de (K. Guan).

http://dx.doi.org/10.1016/j.yjmcc.2017.09.008
Received 9 April 2017; Received in revised form 1 September 2017; Accepted 19 September 2017
Available online 21 September 2017

splicing factor RNA-binding motif protein 20 that contains two evolutionary highly conserved functional domains: a RNA-recognition motif 1 (RRM-1) and an arginine/serine-rich (RS-rich) domain. RBM20 plays an important role in assembling spliceosome and regulating alternative splicing of pre-mRNA [2–4]. Several heterozygous missense mutations in *RBM20* including R634Q, R634W, S635A, R636S, R636H, R636C, S637G and P638L, which cause early-onset DCM, were identified in a five amino acid hotspot in the RS-rich domain [2,5–8]. *RBM20* mutations exist in up to 3% of patients with idiopathic DCM, in 5% of confirmed or suspected familial cases and in over 13% of patients with a history of sudden cardiac death. These mutations are associated with a younger age at diagnosis, end-stage heart failure, and a high degree of morbidity and mortality [5,6,8].

RBM20 was identified as the first splicing factor of the sarcomeric protein titin (TTN), a main determinant of diastolic function [2]. Rats with a deletion of exons 2–14 of *Rbm20* revealed many phenotypic features that are observed in patients with DCM related to mutant RBM20 [2]. Besides TTN, a set of 30 genes with conserved alternative splicing regulation between humans and rats were identified to be involved in Rbm20-dependent alternative splicing processes, including genes linked to cardiomyopathy, ion-homeostasis, and sarcomere biology [2]. A Rbm20-knockdown study in mouse embryonic stem cells (ESCs) showed that Rbm20 deficiency in ESC-derived cardiomyocytes (CMs) resulted in impaired sarcomere organization and ion transport in the sarcoplasmic reticulum, coinciding with early disruption of RNA processing [9].

A big hurdle for understanding cardiac molecular and cellular physiology is the general unfeasibility to maintain and study functional human CMs in culture. Given the ability to generate and cultivate human induced pluripotent stem cells (iPSCs) *in vitro*, patient-specific iPSC-derived CMs (iPSC-CMs) provide a unique opportunity to model heart diseases *in vitro* [10,11].

Here, we hypothesized that iPSC-CMs derived from a DCM patient with the missense mutation S635A in the conserved RS-rich domain of RBM20 can be used to investigate the pathogenesis of mutant RBM20-causing DCM at cellular and molecular levels. We generated engineered heart muscles (EHMs) from iPSC-CMs and studied their active and passive force generation. The functionality and cell biology of these patient-specific iPSC-CMs as well as EHMs, specifically those related to the cardiac DCM phenotype, would give novel insights into the functional changes during DCM development. Furthermore, splicing factors as RBM20 are attractive targets to develop novel therapeutic and protective strategies on a patient-specific level.

2. Materials and methods

2.1. Patient

The study was approved by the ethical committee of the University Medical Center Göttingen (Az. 21/1/11). A 34-year-old woman characterized by severe DCM and arrhythmias was recruited in this study. The female patient had an early onset of disease at the age of 23 years. Because of syncope and arrhythmias, an automated cardioverter-defibrillator was implanted. At the age of 29 years, she showed a severe symptomatic heart failure (NYHA III). Echocardiographic examination revealed left ventricular dilation with cardiac dysfunction (ejection fraction about 29%). Genetic analysis revealed a heterozygous missense mutation (S635A) in exon 9 of the *RBM20* gene in the patient, as described earlier [2].

2.2. Isolation and cultivation of skin fibroblasts

For the establishment of skin fibroblast culture, skin punch biopsies (3.5–4 mm) were taken aseptically by a surgeon, placed in Dulbecco's modified Eagle's medium (DMEM; Thermo Fisher Scientific) containing penicillin (100 U/ml)/streptomycin (100 µg/ml) (Thermo Fisher Scientific), transferred as soon as possible to the lab and cut into pieces of 1–1.5 mm side length. The pieces were then placed epidermis upside in cell culture dish and cultured in fibroblast growth medium composed of DMEM supplemented with 10% fetal calf serum (FCS; selected batch, Lonza), 1 × non-essential amino acids (NEAA; Thermo Fisher Scientific), glutamine (2 mM; Thermo Fisher Scientific), β-mercaptoethanol (β-ME; 50 µM, Promega), penicillin (50 U/ml)/streptomycin (50 µg/ml) at 37 °C with 5% CO_2 atmosphere without moving the dishes. Fibroblasts grew out from the tissue pieces and were passaged two weeks later. The cells are normally ready for transduction experiments before passage 3 (p3).

2.3. Generation, culture and characterization of hiPSCs

Generally, a total of 2–3 × 10^4 fibroblasts from the patient (F-1-RBM20; F-1-R) plated in fibroblast growth medium in one well of a 6-well tissue culture plate were transduced with lentiviral particles as described before [12]. As lentiviral system the STEMCCA cassette was used, which is a humanized excisable system containing all four reprogramming factors *OCT4*, *SOX2*, *KLF4*, and c-*MYC* in a single "stem cell cassette" (pHAGE2-EF1αFull-hOct4-F2A-hKlf4-IRES-hSox2-P2A-hcMyc-W-loxP) [12]. The generated iPSCs were cultured on mitomycin C-inactivated mouse embryonic fibroblasts and propagated by using collagenase IV (200 U/ml, Worthington) in human ESC medium as described previously [12].

For characterization of the generated iPSCs regarding their pluripotency, RT-PCR analysis, immunocytochemical staining, bisulfite sequencing assays, spontaneous differentiation *in vitro* and teratoma formation *in vivo* were carried out using standard protocols as described earlier [12]. For details, please see Supplementary data.

Three independent iPSC lines derived from the patient were designated 1-RBM20-2 (1-R-2), -3 (1-R-3), -7 (1-R-7) (Table S1), characterized for their pluripotency and used in this study. As healthy controls, we used five iPSC lines derived from three healthy donors without known cardiovascular diseases (designated C1-1, C1-2, C2-1, C2-2 and C3-1, respectively) (Table S1).

2.4. Directed differentiation of iPSCs into cardiomyocytes

The generated iPSC lines were adapted from feeder-dependent cultures to feeder-free adherent cultures by cultivating on Geltrex-coated cell culture plates in the presence of chemically defined medium E8 (Thermo Fisher Scientific). Cardiac differentiation of iPSCs was performed by sequential targeting of the Wnt pathway as described previously [13]. Briefly, undifferentiated iPSCs were cultured as a monolayer in E8 medium on Geltrex-coated 12-well plates. At 85%–95% confluence, the differentiation was initiated by changing the medium to RPMI 1640 (Thermo Fisher Scientific) supplemented with 2 mM L-glutamine, 1 × B27 without insulin (Thermo Fisher Scientific) and the GSK3β inhibitor CHIR99021 (10 µM, Millipore) (d0). After 48 h, medium was changed to fresh media supplemented with 5 mM of the Wnt signaling inhibitor IWP2 (Millipore) for two days. From day 8 on, the cells were cultured in cardio culture medium containing RPMI 1640 supplemented with 2 mM L-glutamine and 1 × B27 with insulin (Thermo Fisher Scientific), with a medium change every 2–3 days. CMs were purified using metabolic selection [14] and studied on day 60 after initiation of differentiation except when mentioned otherwise.

2.5. Surface area measurement of iPSC-CMs

On day 60 after differentiation, the single iPSC-CMs were immunostained with antibodies against α-actinin, cardiac troponin T (cTNT), and ventricular isoform of the myosin light chain 2 (MLC2V), and images were made using a fluorescence microscope (Zeiss Observer Z1). The surface areas of the single iPSC-CMs were measured by using computerized morphometric system (ImageJ software, NIH Bethesda).

2.6. Measurement of sarcomeric regularity in iPSC-CMs

Images of single iPSC-CMs stained for α-actinin were processed by a custom routine in ImageJ for quantitative analysis of sarcomere organization. To get proper measurements of sarcomere organization, the striation pattern of the α-actinin staining was first aligned vertically within the field of view. The sarcomere organization was quantitated from a user-defined region of interest (ROI) with sarcomeres. The 2D fast Fourier transform (FFT) of images was processed as described previously [15] for un-patterned images, the 2D Fourier spectra were converted to 1D representations by summing up the radial profiles of the 2D FFT resulting in a series of peaks localized at integer multiples of the spatial frequency of the sarcomeric pattern. The amplitude of the first-order peak is a measure of sarcomere regularity, as the organization increases as more sarcomeric α-actinin-positive elements are localized regularly at a distance of the sarcomere length [15].

2.7. Measurement of calcium transients in iPSC-CMs

For intracellular Ca^{2+} transient recordings, both control- and RBM20-iPSC-CMs around day 60 were digested, plated on Geltrex-coated glass coverslips and incubated in cardio culture medium for one week before use. For Ca^{2+} imaging, iPSC-CMs were first incubated with 5 μM Fura-2-AM (Thermo Fisher Scientific) for 30 min. Following incubation, cells were washed once and incubated in cardio culture medium for additional 15 min before measurements were started to enable complete de-esterification of intracellular Fura-2 and allow cellular rebalance of Ca^{2+} cycling properties. Intracellular Ca^{2+} transients in spontaneously beating control- and RBM20-iPSC-CMs were recorded using an IonOptix system (Milton, MA) at 35 °C. Cells were excited at 340 and 380 nm and the emitted fluorescence was collected at 510 nm. The intracellular Ca^{2+} level was measured as the ratio of fluorescence at 340 and 380 nm (340/380 nm). Analysis included the peak amplitude (the Fura-2 ratio at systole subtracted by the Fura-2 ratio at diastole) of Ca^{2+} transients, the area under the curve of Ca^{2+} transients, time to peak, the rising slope, the decay rate (Tau) of Ca^{2+} transients, the duration and the frequency of Ca^{2+} transients. Data files were exported and monotonic transient analysis was performed with the software LabChart Pro (ADInstruments).

2.8. Western blot

For analysis of TTN-isoform composition, pellets of iPSC-CMs or small pieces of left ventricular tissue from an adult human non-failing heart that did not carry any non-synonymous sequence variants in RBM20 were solubilized in a modified Laemmli buffer (8 M Urea, 2 M thiourea, 3% SDS (w/v), 75 mM DTT, 0.03% (w/v) bromophenol blue, 10% (v/v) glycerol, 50 mM Tris-HCl, pH 6.8). Frozen myocardial sample originated from a healthy donor heart that could not be transplanted for technical reasons. The human sample was achieved in compliance with the local ethical committee (Az. 31/9/00), and written informed consent was received from the participant before inclusion. Titin isoforms were separated on agarose-strengthened SDS-polyacrylamide gels (1.8% polyacrylamide, 0.5% agarose) and analyzed as previously described [16]. Protein bands on polyvinylidene difluoride (PVDF) membranes were visualized with Coomassie brilliant blue R. For immuno-detection, antibodies against the N- and C-terminal fragments of titin (Myomedix) were used. ImageJ software was used for densitometry analyses of titin gels and immunoblots.

2.9. Generation and functional phenotyping of engineered heart muscles

Circular EHMs were generated according to the previously published protocol [17,18]. Briefly, 4-week-old beating control- and RBM20-iPSC-CMs (1×10^6/EHM) with the estimated purity in a range of 65% - 80% were selected and mixed carefully on ice with bovine collagen type I (Collagen Solutions LLC) and EHM medium (Iscove's modified Dulbecco's medium, 2 mM L-glutamine, 20% FCS, 1 × NEAA, 0.1 mM β-ME, penicillin (100 U/ml)/streptomycin (100 μg/ml), all from Thermo Fisher Scientific) and then casted into circular molds (inner/outer diameter: 4/8 mm; height: 5 mm; volume: 450 μl). The purity of iPSC-CMs was exemplarily determined by flow cytometry analysis using the antibody against α-actinin. After a 3-day condensation phase, EHMs were transferred onto mechanical stretchers for continuous culture under auxotonic strain and for functional maturation for additional 12–14 days. Culture medium was changed 24 h after EHM casting and then every other day.

Active force generation of EHMs was measured under isometric conditions in continuously gassed (5% CO_2/95% O_2) Tyrode's solution (containing: 120 mM NaCl, 1 mM $MgCl_2$, 0.2 mM $CaCl_2$, 5.4 mM KCl, 22.6 mM $NaHCO_3$, 4.2 mM NaH_2PO_4, 5.6 mM glucose, and 0.56 mM ascorbate). Then a calcium response curve (0.2–4 mM) and stimulation with isoprenaline (1 μM) at half-maximal calcium concentration (EC50) was performed. Passive forces (stress) were recorded as approximation of stiffness by stepwise increasing EHM length (strain) to length of maximal force development at stimulation frequency of 1.5 Hz (field stimulation, pulse width 5 ms, voltage 10% above threshold) and 2 mM calcium concentration. Volume or size measurement of CMs in EHMs was performed by using flow cytometry after the digestion of EHMs into single cells [18]. To measure cross-sectional area (CSA) of EHMs, pictures of each EHM were taken from the frontal and side views while suspended in the organ bath. An average of three readings of frontal width (FW) and side width (SW) of each EHM arm were taken and CSA was calculated according to the following formula: $CSA = FW/2 \times SW/2 \times \pi \times 2$.

2.10. RNA sequencing (RNA-seq) and bioinformatics

Differential gene expression was obtained by use of RNA sequencing performed on an Illumina HighSeq-2000 platform and bioinformatics. Total RNA was isolated from 2-month-old iPSC-CMs from 2 controls with 2 cell lines each (n = 6 samples) and from 2 RBM20-iPSC lines (n = 3 samples) using standard protocols (Promega). 150 ng RNA per sample was subjected to library preparation (TruSeq RNA Library Prep Kit v2, Illumina) and next-generation RNA sequencing using paired-end sequencing (2 × 75 bp, > 40 Mio reads/sample) by the application of Illumina HiSeq2000 platform.

The analysis of RNA-seq data was performed as described previously [19]. In brief, RNA-seq data were aligned to the genome using gapped alignment as RNA transcripts are subject to splicing and reads might therefore span two distant exons. Reads were aligned to the whole *homo sapiens* hg19 genome using STAR aligner (2.3.0e_r291) with default options, generating mapping files (BAM format). Read counts for all genes and all exons (Ensembl annotation v74) were obtained using FeaturesCount (http://bioinf.wehi.edu.au/featureCounts/). Read counts for differentially expressed genes (DEGs) were generated and the samples from different groups were compared using DESeq2 [20]. Genes with a Benjamin and Hochberg–adjusted P value (false discovery rate) of < 0.05 were considered to be differentially expressed. Read counts for differentially expressed exons (DEEs) or differential exon usage were generated and the samples from different groups were compared using DEXSeq. Exons with an adjusted P value < 0.1 were considered to be differentially expressed. Gene ontology (GO) enrichment analysis of bioprocesses was performed with GOSeq [21].

2.11. Statistical analysis

To compare sarcomeric structure, cell surface area, Ca^{2+} transient properties, TTN alternative splicing and gene expression, data that passed tests for normality were analyzed with the use of Student's *t*-test. Two-sided P values of < 0.05 were considered statistically significant. For comparison of force of contraction and stress strain curve of EHMs,

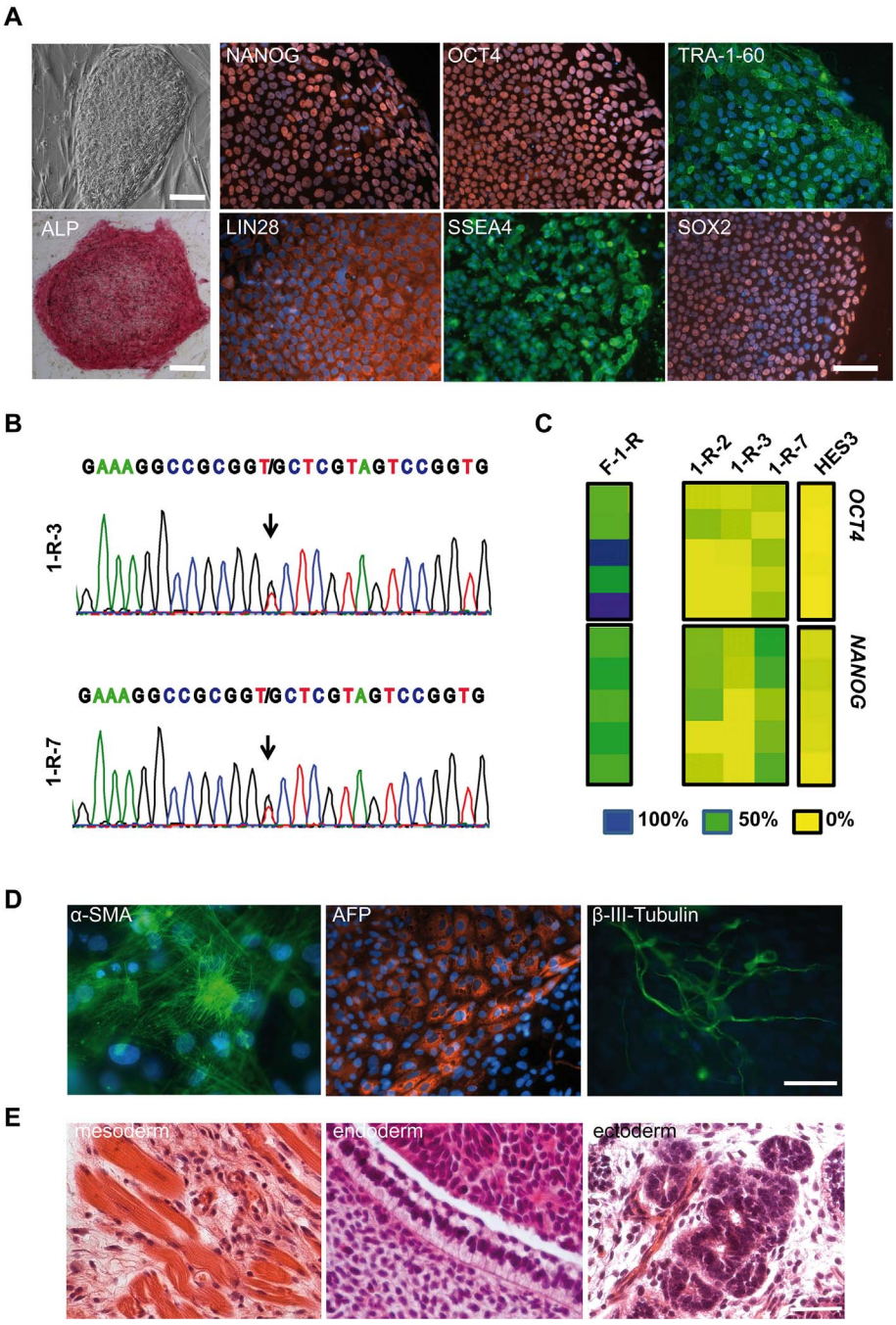

Fig. 1. Proof of pluripotency and spontaneous differentiation capacity of RBM20-iPSCs. A, the generated RBM20-iPSC lines with typical morphology for human pluripotent stem cells expressed alkaline phosphatase (ALP) and were positive for pluripotency markers NANOG, OCT4, TRA-1-60, LIN28, SSEA4, and SOX2 as demonstrated by immunofluorescence staining. The cells were counterstained with DAPI (blue). Scale bars, 100 µm. B, the expected RBM20 mutation leading to the amino acid substitutions S635A was confirmed in the generated iPSCs by DNA sequencing. C, bisulfite sequencing analysis of DNA methylation of *OCT4* and *NANOG* promoter regions. Color codes indicate 0% (yellow), over 50% (green) to 100% (blue) methylation. The y-axis shows individual CpGs analyzed. The x-axis shows different cell types analyzed. HES3 was used as a positive control. F-1-R are fibroblasts from the RBM20 patient before reprogramming. All other cell lines are iPSCs from the patient. D, immunofluorescence staining of *in vitro* differentiated cells from RBM20-iPSCs using antibodies against tissue-specific markers α-SMA (mesoderm), AFP (endoderm), and β-III-tubulin (ectoderm). The cells were counterstained with DAPI (blue). Scale bar, 100 µm. E, teratoma formation of RBM20-iPSCs in immunodeficient mice. Shown are striated muscles (mesoderm), epithelium with intestinal differentiation (endoderm), and neural tissues (ectoderm). Scale bar, 50 µm. (A, D, E) Shown are representative images for one cell line of the RBM20 patient.

the two-way ANOVA was used. The statistical software used for analysis was Graph pad prism (version 6). All data are reported as means ± standard error of the mean (SEM).

3. Results

3.1. Generation of patient-specific iPSC lines

We derived iPSCs from dermal fibroblasts (F-1-R) of the patient with the heterozygous S635A mutation in *RBM20*. Three independent RBM20-iPSC lines (1-R-2, -3, and -7) were generated and analyzed for their pluripotency. They showed the typical human pluripotent stem cell morphology and were positive for alkaline phosphatase (ALP; Fig. 1A). DNA sequencing confirmed the expected mutation in the generated RBM20-iPSC lines (Fig. 1B). RT-PCR analysis showed that RBM20-iPSCs, similar to human ESCs (HES3), expressed pluripotency markers like *OCT4*, *NANOG*, *LIN28*, and *SOX2* (Fig. S1A) and bisulfite sequencing revealed more demethylated promoter regions of *OCT4* and *NANOG* in the generated RBM20-iPSC lines compared to their parental fibroblasts (Fig. 1C). In addition, all RBM20-iPSC lines were positive for human pluripotent stem cell markers NANOG, OCT4, TRA-1-60, LIN28, SSEA4, and SOX2 as demonstrated by immunocytochemical staining (Fig. 1A). Differentiation potential of each RBM20-iPSC line was tested *in vitro via* embryoid body (EB)-mediated differentiation (Figs. 1D, S1B) and *in vivo via* teratoma formation (Fig. 1E). All RBM20-iPSC lines differentiated into derivatives of three embryonic germ layers *in vitro*, as detected by expression of genes specific for mesoderm, α-myosin heavy chain (*MYH6*) and *MLC2V*, for endoderm, α-fetoprotein (*AFP*) and albumin (*ALB*), and for neuroectoderm, tyrosine hydroxylase (*TH*) (Fig. S1B). On protein level, smooth muscle α-actin (α-SMA) for

mesodermal tissue, AFP for endodermal and β-III-tubulin for ectodermal tissue were detected (Fig. 1D). Teratoma formation in immunodeficient mice (RAG2$^{-/-}\gamma c^{-/-}$) confirmed *in vivo* differentiation potential of the generated RBM20-iPSC lines by showing striated muscles (mesoderm), epithelium with intestinal differentiation (endoderm), and neural tissues (ectoderm) (Fig. 1E).

3.2. RBM20-iPSC-CMs exhibit an increased heterogeneous sarcomeric organization pattern but show no difference in cell size

The findings of cardiac-specific pathology of RBM20 deficiency [2] caused our interest in studying the pathogenesis of RBM20 DCM using RBM20-iPSC-CMs. Both control- and RBM20-iPSCs were differentiated into CMs (Videos S1) with a purity of > 90% using a standardized protocol [13,14]. Single beating CMs were used for further analysis. We did not observe significant differences in cardiac differentiation capacity between control- and RBM20-iPSCs. The iPSC-CMs from both control and the RBM20 patient expressed high levels of cardiac-specific genes such as *ACTN2, MYH6, MYH7*, and *TNNT2* whereas the expression of pluripotency genes (*SOX2*, and *LIN28*) was decreased (Fig. S2). In addition, both control- and RBM20-iPSC-CMs expressed the sarcomeric proteins α-actinin, cTNT as well as myosin light chain 2a (MLC2A) and MLC2V (Fig. 2A). However, compared to control-iPSC-CMs at day 60 post differentiation, the majority of RBM20-iPSC-CMs showed a punctate distribution of sarcomeric α-actinin, a major component of the cardiac Z-disk, over the bulk of the total cellular area (Fig. 2A). Quantitative analysis of the regularity of sarcomere organization from the images of single iPSC-CMs stained for α-actinin revealed that RBM20-iPSC-CMs were with a significantly abnormal distribution of sarcomeric α-actinin compared to control-iPSC-CMs ($P < 0.001$; Fig. 2B). This phenotype was consistently observed in two different RBM20-iPSC lines, suggesting a homogeneous correlation to the disease-causing S635A mutation. Furthermore, we analyzed the sarcomeric cTNT structure in RBM20- and control-iPSC-CMs (Fig. 2A) and found only a slight difference between RBM20- and control-iPSC-CMs (data not shown). Notably, when cell surface area was measured,

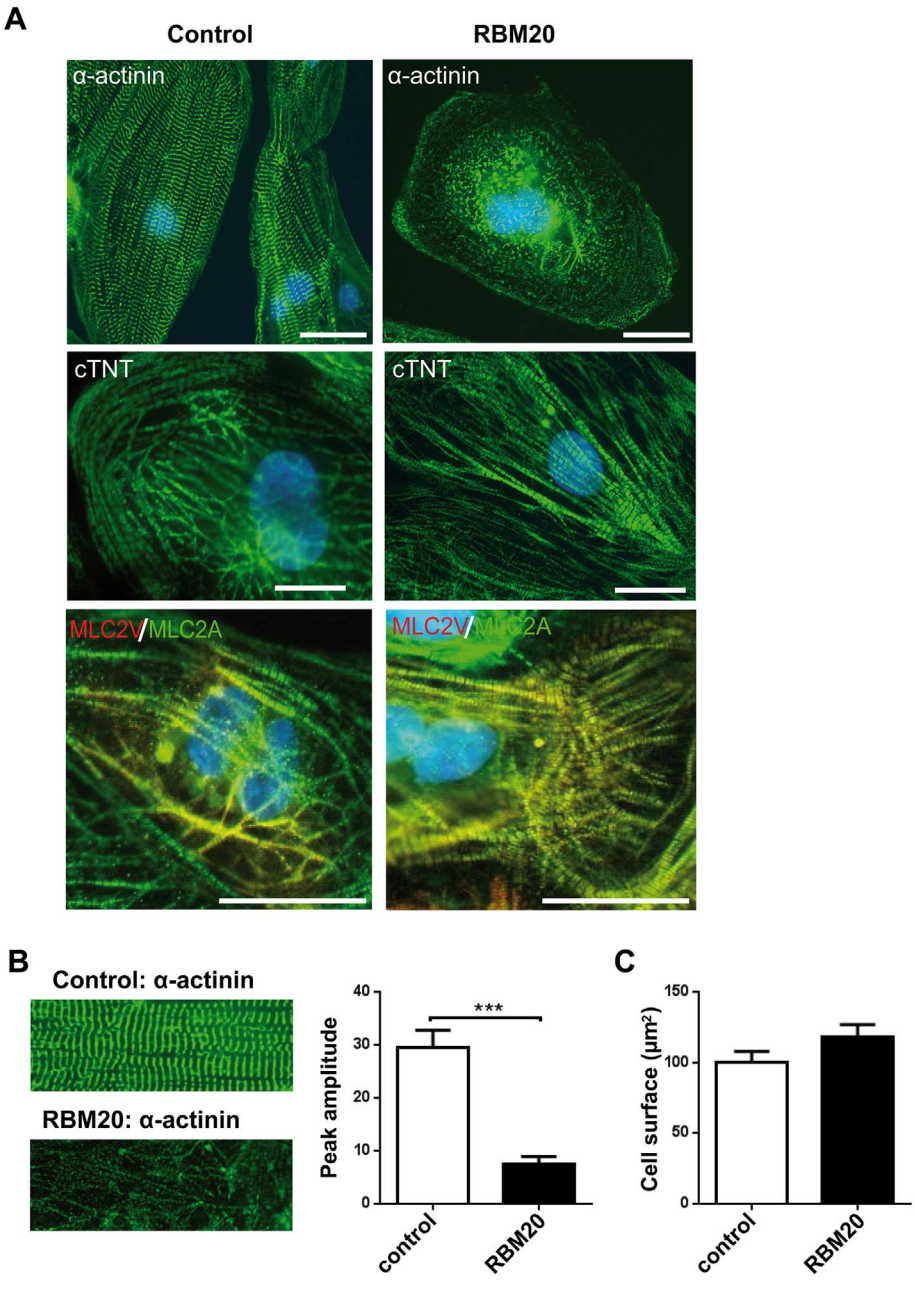

Fig. 2. RBM20-iPSC-CMs exhibited an abnormal distribution of sarcomeric α-actinin. A, immunostaining of sarcomeric α-actinin, cTNT, MLC2A, and MLC2V in iPSC-CMs two months post differentiation. Single RBM20-iPSC-CMs exhibited punctate pattern of sarcomeric α-actinin suggesting a disorganized myofilament structure compared to control-iPSC-CMs (scale bars, 50 µm). No or low difference in sarcomeric assembly was detected by using antibodies against MLC2V, MLC2A, and cTNT, respectively (scale bars, 25 µm). B, enlarged views of small areas of images showing detailed pattern of α-actinin staining in the cells. Using fast Fourier transformation, the striation associated periodic signal amplitude represented by the first spatial frequency was analyzed for both control- and RBM20-iPSC-CMs. Bar graphs summarize the first-order peak amplitude at the spatial frequency. ***$P < 0.001$ RBM20 *vs.* control by Student's *t*-test. C, no significant difference was observed in cell surface between control- (n = 172 CMs from 5 differentiation experiments using C1-1 and 1 experiment using C3-1) and RBM20-iPSC-CMs (n = 117 CMs from 4 differentiation experiments using 1-R-3 and 1 experiment using 1-R-7).

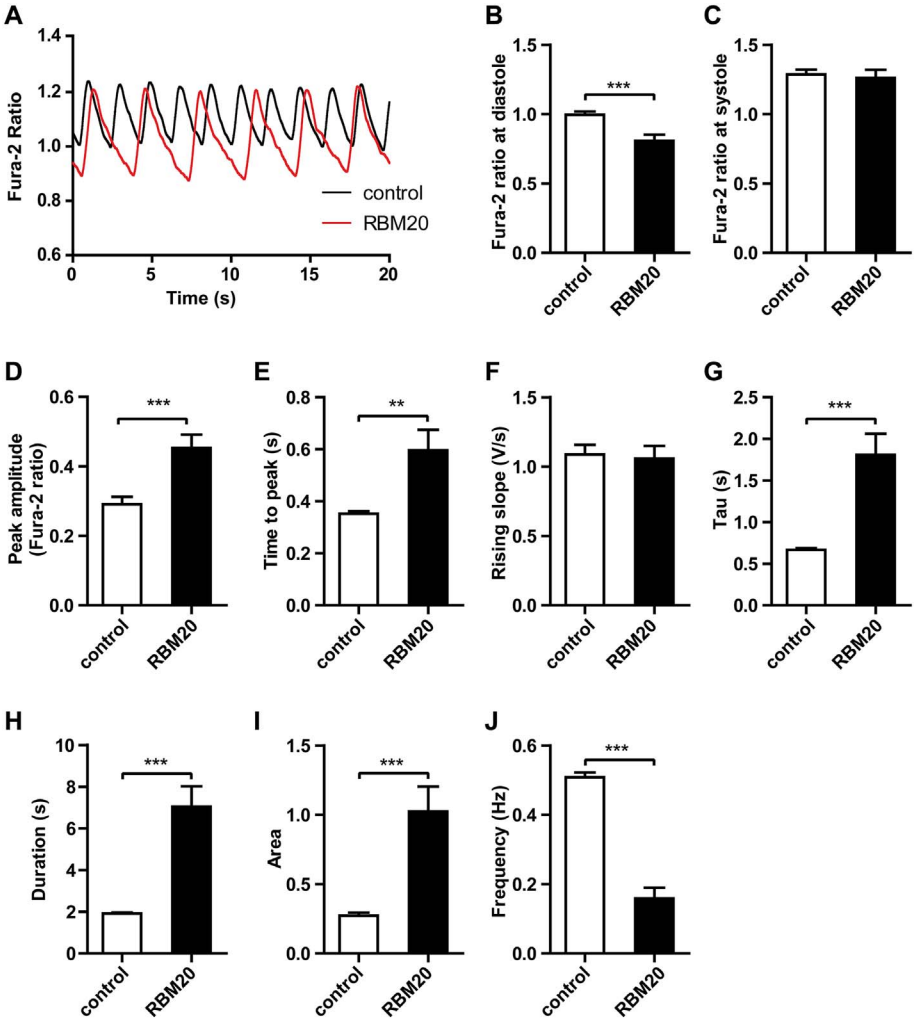

Fig. 3. RBM20-iPSC-CMs showed defective Ca^{2+} cycling. Shown are representative Ca^{2+} tracings in spontaneously beating control- and RBM20-iPSC-CMs (A), diastolic Ca^{2+} levels (B), systolic Ca^{2+} levels (C), peak amplitude of Ca^{2+} transients (D), time to peak (E), the rising slope (F), transient decay rate (τ, G), duration of Ca^{2+} transients (H), average of the area under the curve of Ca^{2+} transients (I), and frequency of Ca^{2+} transients (J). n = 28 CMs from 2 differentiation experiments using control-iPSC lines C1–1 and C1–2; n = 21 CMs from 2 differentiation experiments using RBM20-iPSC lines 1-R-3 and 1-R-7. **P < 0.01; ***P < 0.001 RBM20 *vs*. control by Student's *t*-test.

no significant difference was observed between control- (n = 172 from 6 differentiation experiments) and RBM20-iPSC-CMs (n = 117 from 5 differentiation experiments) (Fig. 2C). These data suggest that RBM20-iPSC-CMs could recapitulate disease phenotypes such as disturbed sarcomere organization, as common in patients with DCM [22].

3.3. RBM20-iPSC-CMs exhibit defective calcium cycling

Defective Ca^{2+} cycling in CMs resulting in impaired muscle contractility is a hallmark of cardiac dysfunction of patients with DCM. To determine the functional consequence of RBM20 deficiency, we measured Ca^{2+} transients in both control- and RBM20-iPSC-CMs. The spontaneously beating RBM20-iPSC-CMs, when compared to control-iPSC-CMs, showed an increase in the peak amplitude of Ca^{2+} transients with lower resting diastolic Ca^{2+} levels, but similar systolic Ca^{2+} levels (Fig. 3A–D), indicating that more Ca^{2+} is released during each contraction-relaxation cycle in RBM20-iPSC-CMs. The rising time (time to peak) was longer without altering the rising rate (Fig. 3E, F). However, the Ca^{2+} transient decay rate (τ), mostly dependent on the activity of Ca^{2+} reuptake by the sarcoplasmic reticulum, was significantly increased in RBM20-iPSC-CMs compared with control-iPSC-CMs (1.807 ± 0.25 s *vs*. 0.667 ± 0.20 s, P = 0.0002; Fig. 3G). Additionally, an increase in the duration of Ca^{2+} transients was observed in RBM20-iPSC-CMs compared with control-iPSC-CMs (Fig. 3H), indicating defective calcium reuptake and cycling. In correlation with these data, we also observed a significant larger area under the curve of Ca^{2+} transients (Fig. 3I) and a lower frequency of Ca^{2+} transients in RBM20-iPSC-CMs compared with control-iPSC-CMs (Fig. 3J).

3.4. Engineered heart muscles generated from RBM20-iPSC-CMs reveal patient-specific RBM20 DCM phenotypes

Because patients with RBM20 mutations develop DCM, we asked whether we could replicate the contractile pathophysiology of DCM in an *in vitro* model of EHM generated from RBM20-iPSC-CMs (Video S2). Consistent with the findings of cell surface area measured in the single iPSC-CMs (Fig. 2C), the RBM20 mutation had no effect on the volume (or size) of CMs in EHMs (data not shown). The amount of CMs (α-actinin-positive cells) as muscle content after EHM generation was similar in both RBM20- and control-EHMs (Fig. S3A). Cross sectional area (CSA) of EHMs generated from RBM20-iPSC-CMs was also comparable to control-EHMs (Fig. 4A). However, RBM20-EHMs showed an impaired force of contraction (FOC) in comparison to control-EHMs (Figs. 4B, S3B). EHMs from both RBM20- and control-iPSC-CMs showed a comparable inotropic response to β-adrenergic stimulation with isoprenaline (Fig. 4C). Interestingly, not only active force generation was reduced in RBM20-EHMs (Fig. 4B), but also passive stress of the tissue was decreased in response to stepwise increases in strain (Fig. 4D), suggesting a higher visco-elasticity of RBM20-EHMs.

3.5. TTN alternative splicing is influenced during early development in RBM20-iPSC-CMs

Titin normally undergoes a series of isoform expression changes

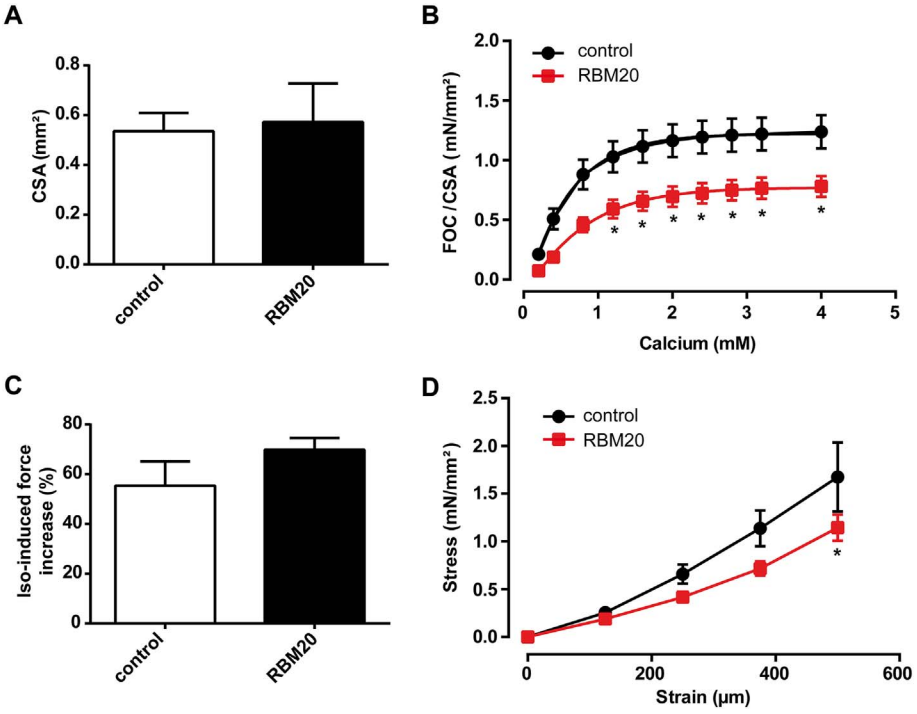

Fig. 4. Functional phenotype of RBM20-EHMs. A, cross sectional area (CSA) of EHMs from RBM20- and control-iPSC-CMs. B, force of contraction per cross sectional area (FOC/CSA) of EHMs in response to increasing extracellular calcium concentration (0.2–4 mM) to assess the maximal inotropic capacity of EHMs. C, inotropic response of EHMs from RBM20- and control-iPSC-CMs to stimulation with 1 µM isoprenaline (Iso). D, stress-strain curve of EHMs from RBM20- and control-iPSC-CMs. A-D: n = 13 control-EHMs generated from 5 independent differentiation experiments with control iPSC lines C1-1 and C3-1; n = 11 RBM20-EHMs generated from 3 independent differentiation experiments with RBM20-iPSC lines 1-R-2 and 1-R-3. *P < 0.05 RBM20 *vs.* control by two-way ANOVA (B, D).

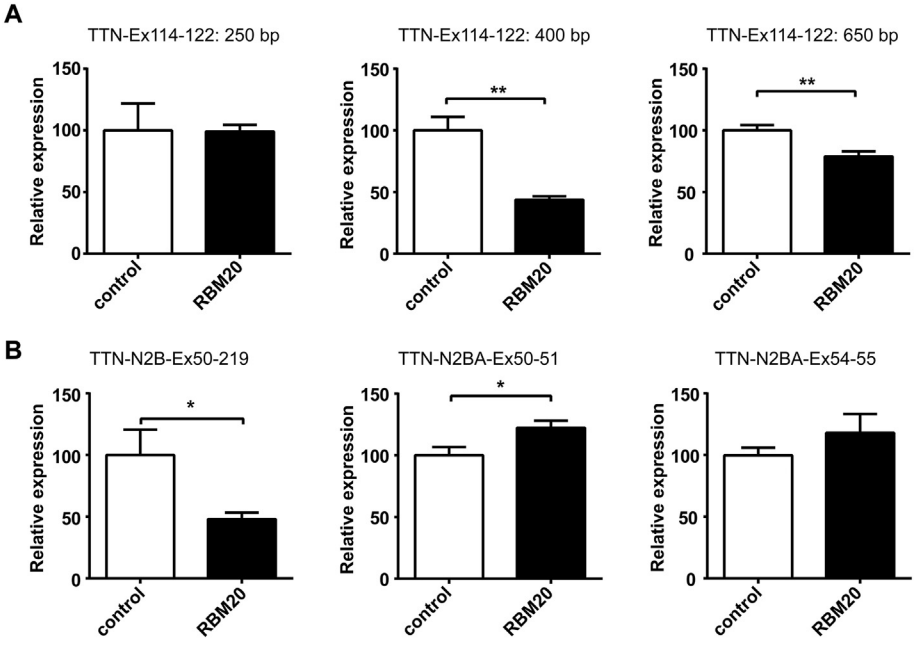

Fig. 5. TTN alternative splicing and isoform proportion are affected in RBM20-iPSC-CMs. A, *TTN* alternative splicing is influenced during early development in RBM20-iPSC-CMs. RT-PCR analysis of RBM20- and control-iPSC-CMs at day 60 of differentiation and relative densitometry were performed to detect the TTN alternative splicing variants with sizes of 250 bp, 400 bp, 650 bp, and 800 bp. The expression of TTN short isoforms of 400 bp and 650 bp relative to the long 800 bp TTN isoform is significantly decreased in RBM20-iPSC-CMs compared to control-iPSC-CMs. Primers (TTN-Ex114-122) were designed to amplify TTN exons from 114 to 122. For RBM20-iPSC-CMs, n = 5 independent differentiation experiments from 2 different cell lines 1-R-3 and 1-R-7 were analyzed. For control-iPSC-CMs, n = 8 independent differentiation experiments from 3 different cell lines C1-1, C2-1 and C2-2 were studied. B, expression of the *TTN-N2B* isoform is reduced and expression of the *N2BA* variants are enhanced in RBM20-iPSC-CMs. Primers spanning TTN exons 49 and 50 (TTN-Ex49-50) were designed for amplifying total TTN, which was used as internal control. For expression of *N2B*, a primer pair spanning exons 50 and 219 (TTN-N2B-Ex50-219) was used. For *N2BA* variants, primers were designed spanning exons 50-51 (TTN-N2BA-Ex50-51) and 54-55 (TTN-N2BA-Ex54-55). The same control- and RBM20-iPSC-CM samples were used as shown in A. For RBM20-iPSC-CMs, n = 5 independent differentiation experiments from 2 different cell lines 1-R-3 and 1-R-7 were analyzed. For control-iPSC-CMs, *n* = 7 independent differentiation experiments from 3 different cell lines C1-1, C2-1 and C2-2 were studied. *P < 0.05; **P < 0.01 RBM20 *vs.* control by Student's *t*-test.

during development as a result of alternative splicing [23–25]. Previous studies showed that the *Rbm20* deletion in heterozygous or homozygous rats alters the isoform expression of TTN, which is due to altered TTN mRNA alternative splicing [2,24]. We studied here whether the RBM20 mutation S635A has a similar effect on TTN alternative splicing in iPSC-CMs. Primers were designed spanning exons 114-122 of TTN, coding for part of the elastic PEVK region [3], to confirm the inclusion of exons in TTN by RT-PCR. Our data revealed a significantly decreased expression of the smaller products with 400 bp and 650 bp in RBM20-iPSC-CMs compared to control-iPSC-CMs (Fig. 5A, S4A). The long product (800 bp) with less exon skipping was used as internal control (Figs. 5A, S4A). DNA-sequencing of the 400 bp band in control-iPSC-CMs confirmed the expected short TTN isoform (data not shown). These data indicate that the exon skipping in the PEVK region of TTN is reduced in RBM20-iPSC-CMs harboring the RBM20 mutation S635A.

3.6. The switch of TTN isoforms is inhibited in RBM20-iPSC-CMs

To determine whether the isoform switch of TTN is influenced by the RBM20 mutation S635A, we analyzed the mRNA expression of titin isoforms (Fig. 5B) and protein proportions (Fig. 6) in two-month-old iPSC-CMs. Primers spanning exons 49 and 50 were designed to quantify total cardiac TTN (N2B and N2BA) used as internal control since these exons are constitutively expressed in both isoforms [26,27]. mRNA

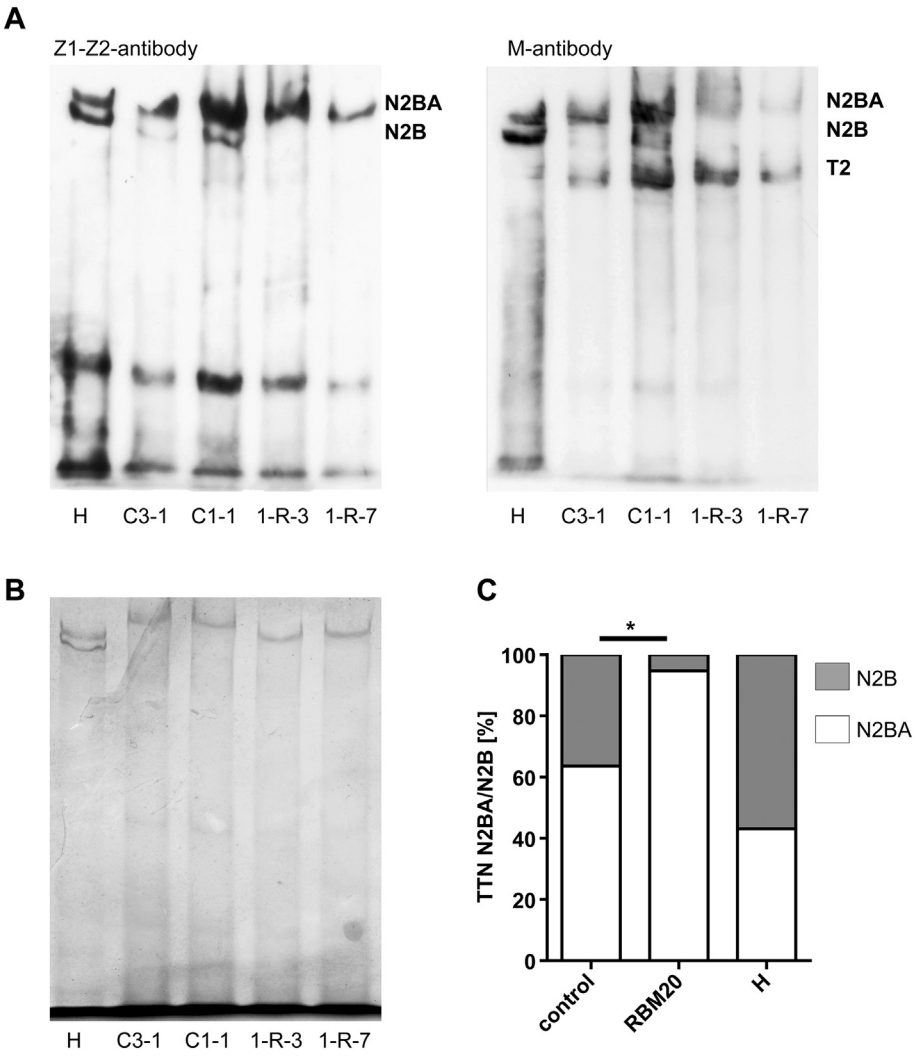

Fig. 6. Expression of cardiac TTN isoforms in RBM20-iPSC-CMs. A, protein expression of TTN isoforms analyzed by Western blot experiments using antibodies against the Z1–Z2 domains at the NH2-terminus, and the M-band region at the COOH-terminus of titin, respectively. The antibody against Z-disk detects, in addition to the isoforms N2BA and N2B, 1-2 lower-mass degradation bands containing I-band of titin. The antibody against M-band detects, in addition to the isoforms N2BA and N2B, the T2/Cronos TTN products. Differentiated iPSC-CMs at day 60 from the RBM20 patient (1-R-3, 1-R-7), and control (C1-1, C3-1) were used for analysis; shown are only two differentiation experiments per condition. B, shown is the Coomassie staining of a PVDF membrane before used for Western blot as loading control. C, densitometry data showing the decreased N2B protein proportion in RBM20-iPSC-CMs (n = 4 independent differentiation from 2 cell lines 1-R-3 and 1-R-7) in comparison to control-iPSC-CMs (n = 6 independent differentiation from 2 cell lines C1-1 and C3-1). H indicates an adult human non-failing heart included as a control (n = 4 technical replicates). *P < 0.05 RBM20 *vs.* control by Student's *t*-test.

expression of the mature *N2B* isoform was analyzed by the use of a primer pair spanning exons 50 and 219. We were able to show that control-iPSC-CMs express the mature *N2B* isoform, which was calculated with 100%. However, *TTN-N2B*-mRNA was significantly reduced in RBM20-iPSC-CMs (Figs. 5B, S4B). Two splicing variants (Ex50-51 and Ex54-55) of the *N2BA* isoform (estimated using primers spanning exons 50-51 or 54-55) were also measured. In contrast to *TTN-N2B* expression, expression of both Ex50-51 and Ex54-55 was significantly increased to 122% (Ex50-51) and to 118% (Ex54-55) in RBM20-iPSC-CMs compared to control-iPSC-CMs, respectively (Figs. 5B, S4B). These results are consistent with protein expression of TTN isoforms in RBM20- and control-iPSC-CMs. In control-iPSC-CMs, we showed the expression of both TTN isoforms N2B and N2BA in 6 out of 6 different experiments, similar to the pattern found in the heart tissue of healthy individuals. In RBM20-iPSC-CMs (n = 4 differentiation experiments), the mature N2B isoform was consistently less expressed (Fig. 6A). Furthermore, we quantitatively analyzed the protein proportion of TTN isoforms in RBM20-CMs and control-CMs (Fig. 6C). Healthy adult human hearts express 60% to 70% N2B and 30% to 40% N2BA isoforms [28]. In the human healthy heart tissue used in this study, 57% N2B and 43% N2BA TTN isoforms (n = 4 different gels analyzed) were expressed (Fig. 6C). In control-iPSC-CMs, we showed the expression of TTN isoform N2B with 39% and N2BA with 61% (n = 6). This protein proportion of TTN isoforms was impaired in RBM20-iPSC-CMs and the expression of the N2B isoform was only 5.3% (n = 4) (Fig. 6C), suggesting that the switch of TTN isoforms was inhibited in RBM20-iPSC-CMs. These results were obtained by using different antibodies recognizing the Z1-Z2 axis at the N-terminus of titin or the M-band at the C-terminal part of titin (Fig. 6A).

3.7. Effects of the RBM20 mutation S635A on gene expression and differential exon usage

We performed RNA-seq analysis to further assess RBM20-dependent splicing and gene expression in iPSC-CMs. Comparison of transcriptome profiles of control- and RBM20-iPSC-CMs revealed 161 differentially expressed genes (DEGs; Fig. 7A, Table S3). *RBM20* itself is not differentially regulated in RBM20-iPSC-CMs compared to control-iPSC-CMs. The 50 most regulated DEGs are shown in a heat map (Fig. 7B). In order to estimate the inter-individual genetic variance and the effect it could have on gene expression differences, we subjected the samples to principal component analysis (PCA). As shown in Fig. 7C, the control samples cluster together, while the disease samples form a clearly distinct cluster across the two dimensions shown. We therefore assume that the main effect of the differential expression analysis results from the disease genotype and not from inter-individual genotypic differences. GO enrichment analysis of DEGs identified genes with key functions, including cellular components as stress fiber (*MYLK*, *TEK*, *UNC13D*), negative regulation of protein depolymerization (*FGF13*, *MID1*, *SCIN*, *SHROOM2*), drug metabolism (*ADH1B*, *GSTT2*, *UGT2B15*), intercalated disc (*DES*, *DSC2*, *DSG2*, *FGF13*), glycosaminoglycan metabolic process (*BGN*, *CSGALNACT1*, *CYTL1*, *EGFLAM*, *FGF13*, *GPC3*,

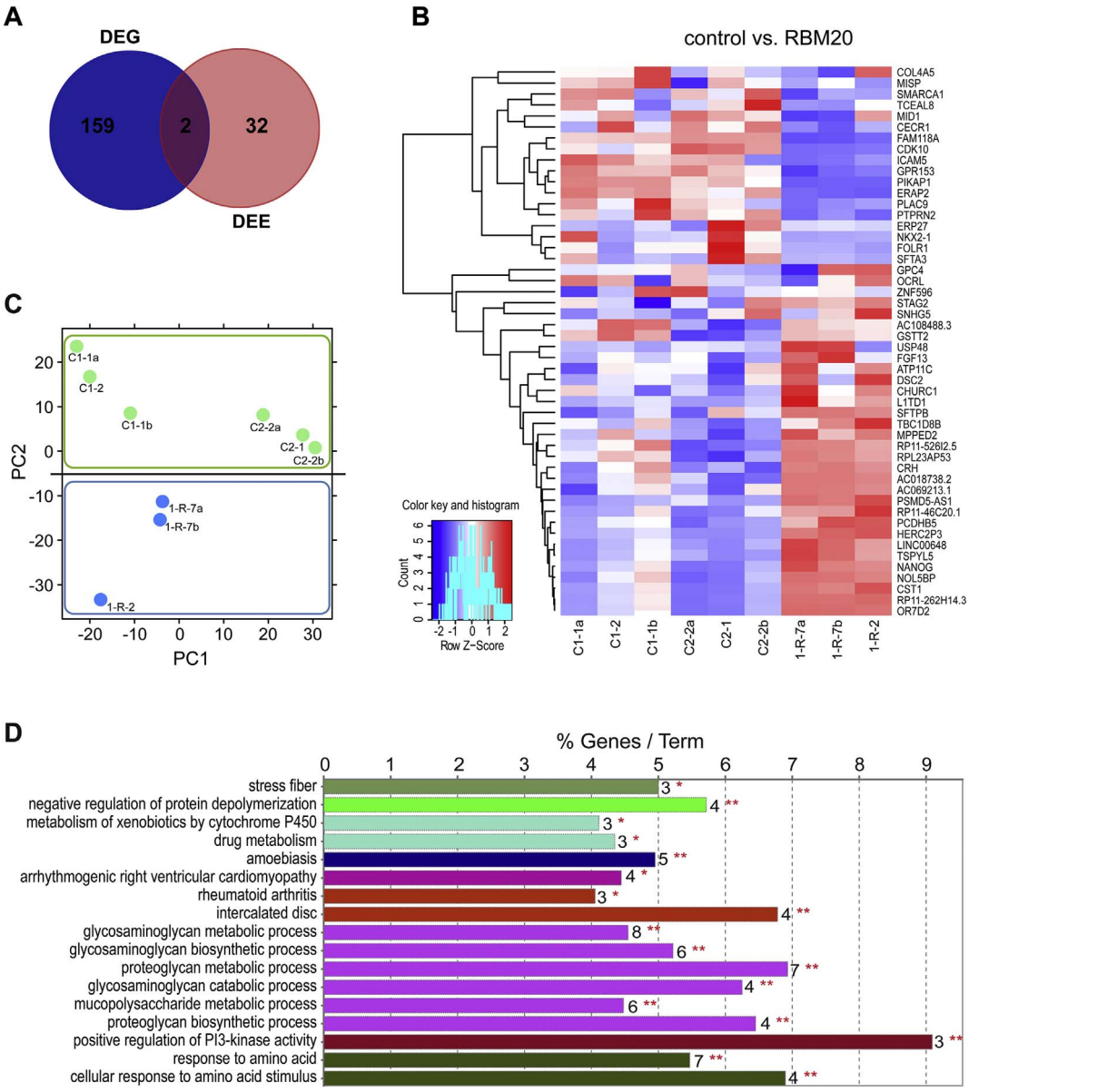

Fig. 7. Modulation of gene expression in RBM20-iPSC-CMs. A, shown are the differentially expressed genes (DEGs) and exons (DEEs) in RBM20-iPSC-CMs compared to control-iPSC-CMs illustrated in a Venn diagram. Only 2 genes were found to be differentially expressed on both gene and exon level. B, heat map of the 50 genes that are most differentially expressed between control- and RBM20-CMs. C, PCA plot of control- and RBM20-iPSC-CM samples used for the analysis. D, significant enriched GO/Pathways in RBM20-iPSC-CMs compared to control-iPSC-CMs according to ClueGo Cytoscape plugin. The data of differential expression are based on all up- or down-regulated genes. Data are generated by GO cellular component, GO biological process or KEGG pathway analysis. Terms of same color correspond to terms containing similar group of genes. The bars represent the number of the genes from the analyzed cluster found associated with the term, and the label displayed on the bars is the percentage of found genes compared to all the genes associated with the term. *P < 0.1; **P < 0.05 calculated based on hypergeometric distribution from Database for annotation, visualization and integrated discovery (DAVID, v6.7). For control-iPSC-CMs, 6 independent differentiation experiments from 2 cell lines of control 1 (C1-1, C1-2) and 2 cell lines from control 2 (C2-1, C2-2), and for RBM20-iPSC-CMs, 3 independent differentiation experiments from 2 cell lines (1-R-2, 1-R-7) were analyzed.

GPC4, *HS6ST2*), or response to amino acids (*COL4A6*, *CYP21A2*, *DNMT3B*, *FOLR1*, *ICAM1*, *MMP3*, *MUC1*) (Fig. 7D, Table S4).

High-throughput RNA-seq generates information on both gene and exon level, allowing us analyzing our data with respect to differential RBM20-dependent exon usage. We found 34 annotated genes with significant changes in exon usage (DEEs) in RBM20-iPSC-CMs compared to control-iPSC-CMs (Fig. 7A; Table S5). However, there was little overlap between genes affected by altered splicing and genes that were differentially expressed (Fig. 7A). In fact, only 2 out of the 161 DEGs (*FAM118A*, *HERC2P3*) were differently spliced in RBM20-iPSC-CMs. This data indicates that differential gene expression and alternative splicing may affect different signaling pathways. To test this hypothesis, we analyzed the differentially spliced genes for enrichment of functional pathways. GO analysis of 34 genes with DEEs revealed that there was a significant overrepresentation of genes associated with ventricular cardiac muscle tissue development (*MYH7*, *COL14A1*), myosin complex (*MYH7*, *MYL7*, *MYOM1*), ribosomal small subunit biogenesis (*RPS28*, *RPS6*), virion assembly (*DDX6*, *UBC*), or regulation of tumor necrosis factor-mediated signaling pathway (*TNFRSF1A*, *UBC*) (Fig. 8A; Table S6). Of note, only few of these pathways were enriched in gene-set of DEGs (Fig. 7D, Table S3). *Vice versa*, pathways linked to metabolic processes, which dominated the list of DEGs (Fig. 7D), could not be identified within the group of alternatively spliced genes (Fig. 8A). These data suggest that metabolic responses in RBM20-iPSC-CMs might be driven by changes in differential gene expression whereas de-regulation of cardiac tissue development might be mainly attributed

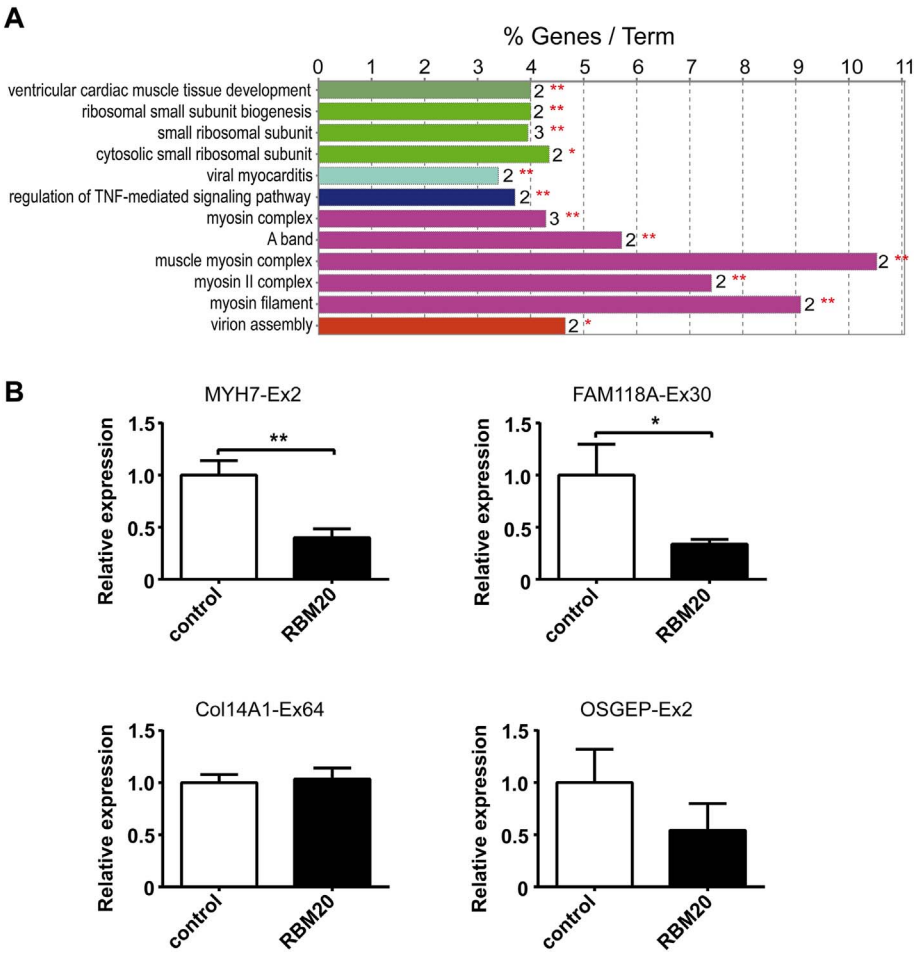

Fig. 8. Alternative splicing changes in RBM20-iPSC-CMs. A, GO enrichment analysis of genes with DEEs reveals divergent cellular pathways affected in RBM20-CMs when compared to control, including ventricular cardiac muscle tissue development, myosin complex, ribosomal small subunit biogenesis and so on. Terms of same color correspond to terms containing similar group of genes. The bars represent the number of the genes from the analyzed cluster found associated with the term, and the label displayed on the bars is the percentage of found genes compared to all the genes associated with the term. *P < 0.1; **P < 0.05 calculated based on hypergeometric distribution from Database for annotation, visualization and integrated discovery (DAVID, v6.7). B, differential expression of specific exons with high adjusted P values as determined by RNA-seq were confirmed by RT-PCR. *P < 0.05; **P < 0.01 RBM20 *vs.* control by Student's *t*-test.

to differential splicing.

Furthermore, we validated some of the DEEs by RT-PCR analysis (Fig. 8B). The downregulation of exon 2 in *MYH7* in RBM20-iPSC-CMs, as shown in DEE data (Fig. S5), was confirmed by the RT-PCR analysis (Fig. 8B). *MYH7* is the gene encoding the myosin heavy chain beta isoform (β-MHC; Fig. S8A). The exclusion of exon 2 of *MYH7* in RBM20-iPSC-CMs suggests a shift towards lower expression of β-MHC. β-MHC plays a major role in cardiac muscle contraction and is specifically implicated in the etiology of DCM, suggesting that RBM20-dependent differential splicing events may be implicated with development of dilative cardiac events.

COL14A1 encodes the alpha chain of type XIV collagen, which is important for growth and structural integrity of the heart during embryonic development [29]. RNA-seq data showed that exon 64 of *COL14A1* was differentially expressed in RBM20-iPSC-CMs compared to control-iPSC-CMs (Table S5; Fig. S6). However, the differential expression of this exon was not confirmed by the RT-PCR analysis (Fig. 8B). Exon 64 of *COL14A1* is used for the expression of both isoforms 3 and 4 of *COL14A1* (Fig. S8B).

Another DEE found in RNA-seq is exon 30 of *FAM118A* (Fig. S7), which was also confirmed by the RT-PCR analysis, and is showing a lower expression in RBM20-iPSC-CMs compared to control-iPSC-CMs (Fig. 8B). Exon 30 of *FAM118A* is exclusively used by isoform 12 of *FAM118A* (Fig. S8C), indicating the downregulation of this isoform in RBM20-iPSC-CMs. GO annotations related to this gene include nucleic acid binding. Interestingly, the DEG data revealed that the expression of *FAM118A* was significantly lower in RBM20-iPSC-CMs as compared to control-iPSC-CMs (Table S3).

For the gene *OSGEP* encoding O-sialoglycoprotein endopeptidase, the RNA-seq data showed its exon 2 as DEE in RBM20-iPSC-CMs (Table S5). The expression of this exon analyzed by RT-PCR showed a trend towards downregulation in RBM20-iPSC-CMs compared to control-iPSC-CMs, but this trend was not significant (Fig. 8B). Exon 2 of *OSGEP* is exclusively used for the expression of protein coding isoform 1 of *OSGEP*.

4. Discussion

In this study, we demonstrate the establishment of a human *in vitro* DCM model by the use of iPSC-CMs from a DCM patient harboring the RBM20 mutation S635A and present evidence that RBM20-iPSC-CMs recapitulate abnormalities, such as cellular and molecular defects found in individuals with RBM20-dependent DCM. We also provide RNA-seq data, which may help us get insights into molecular mechanisms. Our data revealed that the altered post-transcriptional modifications in RBM20-iPSC-CMs might cause the RBM20-dependent DCM in the patient. Notably, by using RBM20-iPSC-CMs in comparison to control-iPSC-CMs we were able to i) show a dysregulated sarcomeric organization and defective calcium handling in RBM20-iPSC-CMs; ii) identify functional characteristics such as altered visco-elasticity and reduced contractile force in RBM20-EHMs; iii) demonstrate an inhibition of TTN alternative splicing and TTN isoform switch in RBM20-iPSC-CMs; and iv) map transcriptome and splicing target profiles of RBM20-iPSC-CMs. These structural and functional differences in iPSC-CMs and -EHMs between control and the patient with the RBM20 mutation S635A are in line with those found in rats with the *Rbm20* deletion and in heart biopsies taken from patients with the RBM20 mutations S635A or P638L [2,4,9]. This indicates that human iPSC-CMs and -EHMs are suitable model systems to study molecular and pathophysiological mechanisms underlying RBM20-dependent DCM.

Our study adds to a recent report demonstrating the ability to model RBM20 DCM using patient-specific iPSCs [30]. To our knowledge, this is the first analysis up to now, where a RBM20-dependent DCM phenotype is modeled not only in a 2D monolayer but also in a 3D culture for analysis of functionality. EHMs are more mature than 2D CMs albeit not like *in vivo* heart muscles [18]. We observed the increased visco-elasticity in RBM20-EHMs that implicates the diastolic function of the heart in RBM20 DCM patients. Previous studies demonstrated that the larger N2BA isoforms caused an increase in titin-based elasticity [16] that has implications for diastolic function and the Frank-Starling mechanism [23,31]. In addition, an increased N2BA/N2B ratio in patients with DCM was shown to correlate with a decreased passive stiffness of cardiomyocytes [32,33]. In our study, we found a reduced active contractile force generation and enhance visco-elasticity (reduced passive tension) in RBM20-EHMs. Our findings are also in line with a study, in which EHMs from iPSC-CMs with the TTN mutation W976R$^{+/-}$ showed a similar phenotype with decreased active contractile force, however, the visco-elasticity was not studied [34].

Importantly, we show for the first time that the mature TTN isoform N2B was consistently less expressed in RBM20-iPSC-CMs on both RNA and protein level. Although iPSC-CMs do not fully recapitulate the cell biology of adult cardiomyocytes [35], we could show that control-iPSC-CMs had a N2BA/N2B ratio of 61:39, nearing that in the adult human heart, which was 43:57 in the present study. However, RBM20-iPSC-CMs showed significant inhibition of the developmental titin-isoform switch, with a N2BA/N2B ratio of 95:5. These data are consistent with the data obtained from the RBM20 knockout rat showing that no N2B isoform was detectable [23] and from the heart biopsy of patients with the RBM20 mutations S635A [2] and E913K showing a shift from the N2B to N2BA isoform [31]. This dramatic increase in TTN N2BA/N2B ratio in RBM20-iPSC-CMs may be directly correlated with the inclusion of exons in the PEVK regions.

RBM20 is predominantly expressed in striated muscle, most highly in the heart, with transcript abundance 4-fold greater in cardiac than in skeletal muscle [2,5]. RBM20 regulates the alternative splicing of a set of genes including TTN as its most sensitive and prominent target [2]. Titin is a sarcomeric protein responsible for maintaining the structure and biomechanical properties of muscle cells [28]. Many mutations in TTN have been reported to be associated with DCM [36,37], and out of them, at least 18 mutations are predicted to have an impact on TTN splicing [38]. RBM20 regulates TTN alternative splicing by mediating exon skipping in the elastic PEVK- and the immunoglobulin-rich regions [3]. We observed that TTN alternative splicing was inhibited in RBM20-iPSC-CMs with the RBM20 mutation S365A by analyzing the expression of exons 114-122 in the PEVK regions (Figs. 5A, S4A). These data are in line with those reported with patient heart biopsies [2,31]. Our data point out an altered TTN alternative splicing already during early cardiogenesis in the RBM20 DCM patient, confirming that RBM20-dependent DCM is an early onset disorder patterned during early heart development and propagated with pathological cardiac remodeling [9].

Taken together, our data demonstrate that altered TTN alternative exon splicing in RBM20-iPSC-CMs may result in the reduced active force generation and the increased visco-elasticity that implicate the diastolic function of the heart in RBM20 DCM patients. The disorganized sarcomeric structures observed in RBM20-iPSC-CMs were reported in previous studies using heart biopsies from patients with the RBM20 mutation P638L or iPSC-CMs from patients with the RBM20 mutation R636S [9,30]. In addition, defective calcium cycling in RBM20-iPSC-CMs were also reported in iPSC-CMs from patients with the RBM20 mutation R636S [30]. These data suggest that the abnormal pattern in sarcomere morphology and defective calcium handling machinery are common in RBM20-dependent DCM pathogenesis. This could in part explain the anatomy and contractile dysfunction of the dilated heart in RBM20 DCM patients.

Using RNA deep-sequencing, RBM20 was shown to be responsible for different transcriptome profiles and involved in alternative splicing of cardiac-specific genes [2,3]. Here, we show that RBM20-iPSC-CMs can be used to detect a dysregulation of a variety of cardiac genes, exons and pathways. We identified 161 DEGs and 34 genes with DEEs in RBM20-iPSC-CMs (*versus* control). However, when we compare our DEGs with the previous study using iPSC-CMs from patients with the RBM20 mutation R636S [30], little overlap has been observed. One explanation could be the profound differences in experimental approaches, where we used 60-day-old iPSC-CMs and Wyles et al. used cells not older than 25 days implying the different maturation stages of the cells used. Interestingly, while a large number of DEGs were found in RNA-seq analysis, only 2 of these (*FAM118A*, *HERC2P3*) were associated with altered splicing. Considering that RBM20 is thought to be involved in regulating splicing, this raises the question why so many genes are differentially expressed but not related to splicing. This could be explained by that the splicing defect affects mainly titin, which is so central to sarcomere integrity, and its disruption leads to multiple secondary changes. Recently, the Seidman lab showed a large number of genes (2237 genes) differentially expressed in 30–40-day old iPSC-CMs carrying a truncated mutation in *TTN* (heterozygous, homozygous N22577 fs) compared to control iPSC-CMs by RNA-seq [34]. However, it is hard to compare these data with ours due to the different rationale behind the studies (*TTN* alternative splicing *vs. TTN* truncation) and the different experiment approaches (different ages of CMs used). Future study could focus on direct comparing RBM20-iPSC-CMs with iPSC-CMs generated from DCM patients with TTN mutations which have an impact on *TTN* splicing only to figure out the primary and secondary gene expression changes related to the RBM20 mutation.

When we analyzed gene and exon expression among the RBM20 group, the most affected pathways for DEGs are metabolic whereas, interestingly, genes with DEEs are associated with cardiac muscle development and myosin complex, including *MYH7*, *MYL7*, *MYOM1* and *COL14A1*. Both *MYH7* and *MYOM1* are directly bound by RBM20 and are identified as direct targets of RBM20 for differential splicing [4]. Differential expression of exon 2 in *MYH7* would suggest an altered expression of β-MHC, which is expressed predominantly in normal human ventricle. Changes in the relative abundance of β-MHC/α-MHC correlate with the contractile velocity of cardiac muscle. These data suggest that metabolic responses in the RBM20-defective CMs are driven by changes in DEGs whereas de-regulation of cardiac tissue development is mainly attributed to differential splicing. We noticed that alternative splicing in some of the targets of RBM20, such as *RYR2*, *CAMK2D* and *LDB3*, as shown in previous publications [2,4,24] has not been identified in our DEE analysis. This might be due to the developmental stage and immature nature of iPSC-CMs. Using real-time PCR, we currently investigate alternative splicing of these genes. Our preliminary data showed that a 24-bp exon in *RYR2* was upregulated in RBM20-iPSC-CMs (our unpublished data), which is in line with the published data shown in *Rbm20*-deficient rats and human cardiomyopathy patients [4]. This 24-bp exon has profound effects on intracellular Ca^{2+} signaling [39]. It is of paramount importance to investigate how RBM20 deficiency affects intracellular Ca^{2+} signaling, which results in contractile deficits. Further studies are also needed to identify more targets of RBM20 using iPSC-CMs.

A limitation of our study is that we have iPSC lines from only one patient with the RBM20 mutation S635A. Since the genetic background and sex of the RBM20 patient and controls can influence the results in this work, isogenic control iPSCs (after correction of the RBM20 mutation) would be ideal and should be used in future studies. Moreover, studying other mutations in the RS-rich domain of RBM20 will validate our findings and figure out the common pathomechanism for RBM20 DCM before development of future molecular diagnostic and therapeutic approaches. Similar to other studies using iPSC-CMs and -EHMs for disease modeling, another limitation of our study is the immature phenotype of iPSC-CMs compared to their *in vivo* counterparts [40]. Furthermore, future studies should focus on the formation of a reproducible tissue design with several cell types (*e.g.* CMs, fibroblasts

and endothelial cells) organized in a way, which mimics human heart.

In conclusion, our studies using iPSC-CMs and -EHMs revealed that the missense variant S635A in RBM20 causes sarcomeric disorganization, defective calcium cycling, retention of the more compliant TTN isoform, N2BA, and differential exon usages of genes related to cardiac muscle function. Collectively, these may directly contribute to substantial contractile deficits. These findings indicate that patient-specific 2D iPSC-CMs coupled with 3D EHMs are suitable for modeling RBM20-dependent DCM and provide robust functional genomic insights, which might help to develop patient-specific therapeutic strategies in the future.

Supplementary data to this article can be found online at https://doi.org/10.1016/j.yjmcc.2017.09.008.

Acknowledgements

We thank Anke Cierpka, Yvonne Wiegräfe, Yvonne Hintz, Sandra Georgi and Johanna Heine for excellent technical assistance.

Funding

This work was supported by the Bundesministerium für Bildung und Forschung (BMBF) grant e:Bio – Modul II – Verbundprojekt: CaRNAtion [031L0075C to K.G., K.S.-B., and G.H.], the German Center for Cardiovascular Research (DZHK) [81X2300106 to K.G. and B.M.], the Heidenreich von Siebold Program from the University Medical Center Göttingen (K.S.-B.), and the German Research Foundation [SFB1002 to K.G., W.A.L., W.H.Z., and G.H. and GU 595/3-1 to K.G.].

Disclosures

None.

References

[1] G.S. Wang, T.A. Cooper, Splicing in disease: disruption of the splicing code and the decoding machinery, Nat. Rev. Genet. 8 (2007) 749–761.
[2] W. Guo, S. Schafer, M.L. Greaser, M.H. Radke, M. Liss, T. Govindarajan, H. Maatz, H. Schulz, S. Li, A.M. Parrish, V. Dauksaite, P. Vakeel, S. Klaassen, B. Gerull, L. Thierfelder, V. Regitz-Zagrosek, T.A. Hacker, K.W. Saupe, G.W. Dec, P.T. Ellinor, C.A. MacRae, B. Spallek, R. Fischer, A. Perrot, C. Ozcelik, K. Saar, N. Hubner, M. Gotthardt, RBM20, a gene for hereditary cardiomyopathy, regulates titin splicing, Nat. Med. 18 (2012) 766–773.
[3] S. Li, W. Guo, C.N. Dewey, M.L. Greaser, Rbm20 regulates titin alternative splicing as a splicing repressor, Nucleic Acids Res. 41 (2013) 2659–2672.
[4] H. Maatz, M. Jens, M. Liss, S. Schafer, M. Heinig, M. Kirchner, E. Adami, C. Rintisch, V. Dauksaite, M.H. Radke, M. Selbach, P.J. Barton, S.A. Cook, N. Rajewsky, M. Gotthardt, M. Landthaler, N. Hubner, RNA-binding protein RBM20 represses splicing to orchestrate cardiac pre-mRNA processing, J. Clin. Invest. 124 (2014) 3419–3430.
[5] K.M. Brauch, M.L. Karst, K.J. Herron, M. de Andrade, P.A. Pellikka, R.J. Rodeheffer, V.V. Michels, T.M. Olson, Mutations in ribonucleic acid binding protein gene cause familial dilated cardiomyopathy, J. Am. Coll. Cardiol. 54 (2009) 930–941.
[6] D. Li, A. Morales, J. Gonzalez-Quintana, N. Norton, J.D. Siegfried, M. Hofmeyer, R.E. Hershberger, Identification of novel mutations in RBM20 in patients with dilated cardiomyopathy, Clin. Transl. Sci. 3 (2010) 90–97.
[7] M.M. Refaat, S.A. Lubitz, S. Makino, Z. Islam, J.M. Frangiskakis, H. Mehdi, R. Gutmann, M.L. Zhang, H.L. Bloom, C.A. MacRae, S.C. Dudley, A.A. Shalaby, R. Weiss, D.M. McNamara, B. London, P.T. Ellinor, Genetic variation in the alternative splicing regulator RBM20 is associated with dilated cardiomyopathy, Heart Rhythm. 9 (2012) 390–396.
[8] Q.S. Wells, J.R. Becker, Y.R. Su, J.D. Mosley, P. Weeke, L. D'Aoust, N.L. Ausborn, A.H. Ramirez, J.P. Pfotenhauer, A.J. Naftilan, L. Markham, V. Exil, D.M. Roden, C.C. Hong, Whole exome sequencing identifies a causal RBM20 mutation in a large pedigree with familial dilated cardiomyopathy, Circ. Cardiovasc. Genet. 6 (2013) 317–326.
[9] R. Beraldi, X. Li, A. Martinez Fernandez, S. Reyes, F. Secreto, A. Terzic, T.M. Olson, T.J. Nelson, Rbm20-deficient cardiogenesis reveals early disruption of RNA processing and sarcomere remodeling establishing a developmental etiology for dilated cardiomyopathy, Hum. Mol. Genet. 23 (2014) 3779–3791.
[10] J. Dudek, I.F. Cheng, A. Chowdhury, K. Wozny, M. Balleininger, R. Reinhold, S. Grunau, S. Callegari, K. Toischer, R.J. Wanders, G. Hasenfuss, B. Brugger, K. Guan, P. Rehling, Cardiac-specific succinate dehydrogenase deficiency in Barth syndrome, EMBO Mol. Med. 8 (2015) 139–154.
[11] K. Takahashi, K. Tanabe, M. Ohnuki, M. Narita, T. Ichisaka, K. Tomoda, S. Yamanaka, Induction of pluripotent stem cells from adult human fibroblasts by defined factors, Cell 131 (2007) 861–872.
[12] K. Streckfuss-Bomeke, F. Wolf, A. Azizian, M. Stauske, M. Tiburcy, S. Wagner, D. Hubscher, R. Dressel, S. Chen, J. Jende, G. Wulf, V. Lorenz, M.P. Schon, L.S. Maier, W.H. Zimmermann, G. Hasenfuss, K. Guan, Comparative study of human-induced pluripotent stem cells derived from bone marrow cells, hair keratinocytes, and skin fibroblasts, Eur. Heart J. 34 (2013) 2618–2629.
[13] X. Lian, J. Zhang, S.M. Azarin, K. Zhu, L.B. Hazeltine, X. Bao, C. Hsiao, T.J. Kamp, S.P. Palecek, Directed cardiomyocyte differentiation from human pluripotent stem cells by modulating Wnt/beta-catenin signaling under fully defined conditions, Nat. Protoc. 8 (2013) 162–175.
[14] S. Tohyama, F. Hattori, M. Sano, T. Hishiki, Y. Nagahata, T. Matsuura, H. Hashimoto, T. Suzuki, H. Yamashita, Y. Satoh, T. Egashira, T. Seki, N. Muraoka, H. Yamakawa, Y. Ohgino, T. Tanaka, M. Yoichi, S. Yuasa, M. Murata, M. Suematsu, K. Fukuda, Distinct metabolic flow enables large-scale purification of mouse and human pluripotent stem cell-derived cardiomyocytes, Cell Stem Cell 12 (2013) 127–137.
[15] W.K. Weiwad, W.A. Linke, M.H. Wussling, Sarcomere length-tension relationship of rat cardiac myocytes at lengths greater than optimum, J. Mol. Cell. Cardiol. 32 (2000) 247–259.
[16] C. Neagoe, M. Kulke, F. del Monte, J.K. Gwathmey, P.P. de Tombe, R.J. Hajjar, W.A. Linke, Titin isoform switch in ischemic human heart disease, Circulation 106 (2002) 1333–1341.
[17] M. Tiburcy, T. Meyer, P.L. Soong, W.H. Zimmermann, Collagen-based engineered heart muscle, Methods Mol. Biol. 1181 (2014) 167–176.
[18] M. Tiburcy, J.E. Hudson, P. Balfanz, S. Schlick, T. Meyer, M.L. Chang Liao, E. Levent, F. Raad, S. Zeidler, E. Wingender, J. Riegler, M. Wang, J.D. Gold, I. Kehat, E. Wettwer, U. Ravens, P. Dierickx, L.W. van Laake, M.J. Goumans, S. Khadjeh, K. Toischer, G. Hasenfuss, L.A. Couture, A. Unger, W.A. Linke, T. Araki, B. Neel, G. Keller, L. Gepstein, J.C. Wu, W.H. Zimmermann, Defined engineered human myocardium with advanced maturation for applications in heart failure modeling and repair, Circulation 135 (2017) 1832–1847.
[19] R. Halder, M. Hennion, R.O. Vidal, O. Shomroni, R.U. Rahman, A. Rajput, T.P. Centeno, F. van Bebber, V. Capece, J.C. Garcia Vizcaino, A.L. Schuetz, S. Burkhardt, E. Benito, M. Navarro Sala, S.B. Javan, C. Haass, B. Schmid, A. Fischer, S. Bonn, DNA methylation changes in plasticity genes accompany the formation and maintenance of memory, Nat. Neurosci. 19 (2016) 102–110.
[20] M.I. Love, W. Huber, S. Anders, Moderated estimation of fold change and dispersion for RNA-seq data with DESeq2, Genome Biol. 15 (2014) 550.
[21] M.D. Young, M.J. Wakefield, G.K. Smyth, A. Oshlack, Gene ontology analysis for RNA-seq: accounting for selection bias, Genome Biol. 11 (2010) R14.
[22] T. Meyer, V. Ruppert, S. Ackermann, A. Richter, A. Perrot, S.R. Sperling, M.G. Posch, B. Maisch, S. Pankuweit, F. German Competence Network Heart, Novel mutations in the sarcomeric protein myopalladin in patients with dilated cardiomyopathy, Eur. J. Hum. Genet. 21 (2013) 294–300.
[23] M.L. Greaser, C.M. Warren, K. Esbona, W. Guo, Y. Duan, A.M. Parrish, P.R. Krzesinski, H.S. Norman, S. Dunning, D.P. Fitzsimons, R.L. Moss, Mutation that dramatically alters rat titin isoform expression and cardiomyocyte passive tension, J. Mol. Cell. Cardiol. 44 (2008) 983–991.
[24] W. Guo, J.M. Pleitner, K.W. Saupe, M.L. Greaser, Pathophysiological defects and transcriptional profiling in the RBM20$^{-/-}$ rat model, PLoS One 8 (2013) e84281.
[25] C.A. Opitz, M.C. Leake, I. Makarenko, V. Benes, W.A. Linke, Developmentally regulated switching of titin size alters myofibrillar stiffness in the perinatal heart, Circ. Res. 94 (2004) 967–975.
[26] M.L. Bang, T. Centner, F. Fornoff, A.J. Geach, M. Gotthardt, M. McNabb, C.C. Witt, D. Labeit, C.C. Gregorio, H. Granzier, S. Labeit, The complete gene sequence of titin, expression of an unusual approximately 700-kDa titin isoform, and its interaction with obscurin identify a novel Z-line to I-band linking system, Circ. Res. 89 (2001) 1065–1072.
[27] C.M. Warren, P.R. Krzesinski, K.S. Campbell, R.L. Moss, M.L. Greaser, Titin isoform changes in rat myocardium during development, Mech. Dev. 121 (2004) 1301–1312.
[28] W.A. Linke, N. Hamdani, Gigantic business: titin properties and function through thick and thin, Circ. Res. 114 (2014) 1052–1068.
[29] G. Tao, A.K. Levay, J.D. Peacock, D.J. Huk, S.N. Both, N.H. Purcell, J.R. Pinto, M.L. Galantowicz, M. Koch, P.A. Lucchesi, D.E. Birk, J. Lincoln, Collagen XIV is important for growth and structural integrity of the myocardium, J. Mol. Cell. Cardiol. 53 (2012) 626–638.
[30] S.P. Wyles, X. Li, S.C. Hrstka, S. Reyes, S. Oommen, R. Beraldi, J. Edwards, A. Terzic, T.M. Olson, T.J. Nelson, Modeling structural and functional deficiencies of RBM20 familial dilated cardiomyopathy using human induced pluripotent stem cells, Hum. Mol. Genet. 25 (2016) 254–265.
[31] A. Beqqali, I.A. Bollen, T.B. Rasmussen, M.M. van den Hoogenhof, H.W. van Deutekom, S. Schafer, J. Haas, B. Meder, K.E. Sorensen, R.J. van Oort, J. Mogensen, N. Hubner, E.E. Creemers, J. van der Velden, Y.M. Pinto, A mutation in the glutamate-rich region of RNA-binding motif protein 20 causes dilated cardiomyopathy through missplicing of titin and impaired Frank-Starling mechanism, Cardiovasc. Res. 112 (2016) 452–463.
[32] I. Makarenko, C.A. Opitz, M.C. Leake, C. Neagoe, M. Kulke, J.K. Gwathmey, F. del Monte, R.J. Hajjar, W.A. Linke, Passive stiffness changes caused by upregulation of compliant titin isoforms in human dilated cardiomyopathy hearts, Circ. Res. 95 (2004) 708–716.
[33] S.F. Nagueh, G. Shah, Y. Wu, G. Torre-Amione, N.M. King, S. Lahmers, C.C. Witt, K. Becker, S. Labeit, H.L. Granzier, Altered titin expression, myocardial stiffness, and left ventricular function in patients with dilated cardiomyopathy, Circulation 110 (2004) 155–162.

[34] J.T. Hinson, A. Chopra, N. Nafissi, W.J. Polacheck, C.C. Benson, S. Swist, J. Gorham, L. Yang, S. Schafer, C.C. Sheng, A. Haghighi, J. Homsy, N. Hubner, G. Church, S.A. Cook, W.A. Linke, C.S. Chen, J.G. Seidman, C.E. Seidman, D.I.S.E.A.S.E. HEART, Titin mutations in iPS cells define sarcomere insufficiency as a cause of dilated cardiomyopathy, Science 349 (2015) 982–986.

[35] R. Zhu, A. Blazeski, E. Poon, K.D. Costa, L. Tung, K.R. Boheler, Physical developmental cues for the maturation of human pluripotent stem cell-derived cardiomyocytes, Stem Cell Res. Ther. 5 (2014) 117.

[36] D.S. Herman, L. Lam, M.R. Taylor, L. Wang, P. Teekakirikul, D. Christodoulou, L. Conner, S.R. DePalma, B. McDonough, E. Sparks, D.L. Teodorescu, A.L. Cirino, N.R. Banner, D.J. Pennell, S. Graw, M. Merlo, A. Di Lenarda, G. Sinagra, J.M. Bos, M.J. Ackerman, R.N. Mitchell, C.E. Murry, N.K. Lakdawala, C.Y. Ho, P.J. Barton, S.A. Cook, L. Mestroni, J.G. Seidman, C.E. Seidman, Truncations of titin causing dilated cardiomyopathy, N. Engl. J. Med. 366 (2012) 619–628.

[37] S. Schafer, A. de Marvao, E. Adami, L.R. Fiedler, B. Ng, E. Khin, O.J. Rackham, S. van Heesch, C.J. Pua, M. Kui, R. Walsh, U. Tayal, S.K. Prasad, T.J. Dawes, N.S. Ko, D. Sim, L.L. Chan, C.W. Chin, F. Mazzarotto, P.J. Barton, F. Kreuchwig, D.P. de Kleijn, T. Totman, C. Biffi, N. Tee, D. Rueckert, V. Schneider, A. Faber, V. Regitz-Zagrosek, J.G. Seidman, C.E. Seidman, W.A. Linke, J.P. Kovalik, D. O'Regan, J.S. Ware, N. Hubner, S.A. Cook, Titin-truncating variants affect heart function in disease cohorts and the general population, Nat. Genet. 49 (2017) 46–53.

[38] C. Chauveau, J. Rowell, A. Ferreiro, A rising titan: TTN review and mutation update, Hum. Mutat. 35 (2014) 1046–1059.

[39] C.H. George, S.A. Rogers, B.M. Bertrand, R.E. Tunwell, N.L. Thomas, D.S. Steele, E.V. Cox, C. Pepper, C.J. Hazeel, W.C. Claycomb, F.A. Lai, Alternative splicing of ryanodine receptors modulates cardiomyocyte Ca2 + signaling and susceptibility to apoptosis, Circ. Res. 100 (2007) 874–883.

[40] T.J. Kolanowski, C.L. Antos, K. Guan, Making human cardiomyocytes up to date: Derivation, maturation state and perspectives, Int. J. Cardiol. 241 (2017) 379–386.